ACS NANO

www.acsnano.org

ARTICLE

Au@AuPd Core-Alloyed Shell Nanoparticles for Enhanced Electrocatalytic Activity and Selectivity under Visible Light Excitation

Kaline N. da Silva, Shwetha Shetty, Sam Sullivan−Allsop, Rongsheng Cai, Shiqi Wang, Jhon Quiroz, Mykhailo Chundak, Hugo L. S. dos Santos, IbrahiM Abdelsalam, Freddy E. Oropeza, Víctor A. de la Peña O'Shea, Niko Heikkinen, Elton Sitta, Tiago V. Alves, Mikko Ritala, Wenyi Huo,* Thomas J. A. Slater, Sarah J. Haigh,* and Pedro H. C. Camargo*

Cite This: *ACS Nano* 2024, 18, 24391−24403

Read Online

ACCESS | Metrics & More | Article Recommendations | Supporting Information

ABSTRACT: **Plasmonic catalysis has been employed to enhance molecular transformations under visible light excitation, leveraging the localized surface plasmon resonance (LSPR) in plasmonic nanoparticles. While plasmonic catalysis has been employed for accelerating reaction rates, achieving control over the reaction selectivity has remained a challenge. In addition, the incorporation of catalytic components into traditional plasmonic-catalytic antenna-reactor nanoparticles often leads to a decrease in optical absorption. To address these issues, this study focuses on the synthesis of bimetallic core@shell Au@AuPd nanoparticles (NPs) with ultralow loadings of palladium (Pd) into gold (Au) NPs. The goal is to achieve NPs with an Au core and a dilute alloyed shell containing both Au and Pd, with a low Pd content of around 10 atom %. By employing the (photo)electrocatalytic nitrite reduction reaction (NO_2RR) as a model transformation, experimental and theoretical analyses show that this design enables enhanced catalytic activity and selectivity under visible light illumination. We found that the optimized Pd distribution in the alloyed shell allowed for stronger interaction with key adsorbed species, leading to improved catalytic activity and selectivity, both under no illumination and under visible light excitation conditions. The findings provide valuable insights for the rational design of antenna-reactor plasmonic-catalytic NPs with controlled activities and selectivity under visible light irradiation, addressing critical challenges to enable sustainable molecular transformations.**

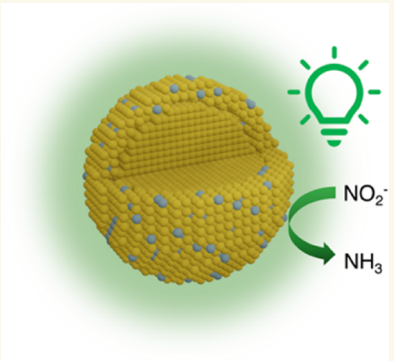

KEYWORDS: *plasmonic electrocatalysis, nitrite reduction reaction (NO_2RR), bimetallic nanoparticles, Au@AuPd core−shell, selectivity, visible light irradiation, ultralow loading*

Plasmonic catalysis is a growing field within photocatalysis, enabling one to harvest visible or near-infrared light to accelerate molecular transformations because of the localized surface plasmon resonance (LSPR) excitation in plasmonic nanoparticles (NPs).[1,2] Plasmonic catalysis has been applied to provide enhanced catalytic activity for reactions such as hydrogenation, reduction, oxidation, and coupling.[3,4] Yet, to take advantage of the full potential of plasmonic catalysis for enhancing reaction rates, more work is needed to better control the selectivity of these systems.[5−7] To achieve this control, a better understanding of the factors that lead to changes in the selectivity under LSPR excitation is needed. Tuning the catalytic function of plasmonic nanoparticles is challenging because common plasmonic materials are limited in the number of reactions to which they may demonstrate excellent catalytic activity and selectivity.[5,8,9] In order to circumvent this problem, hybrid plasmonic-catalytic antenna-reactor NPs have been employed.[10−13] Here, the plasmonic component harvests energy from visible light through the LSPR (generating excited hot chargers and localized heating), which is harvested or transferred to the catalytic sites to drive a specific molecular transformation.[14−16]

Core−shell, core−satellite, and alloys (Figure 1A−C, respectively) represent the state-of-the-art designs for

Received: May 28, 2024
Revised: August 12, 2024
Accepted: August 13, 2024
Published: August 20, 2024

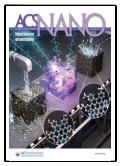

https://doi.org/10.1021/acsnano.4c07076
ACS Nano 2024, 18, 24391−24403

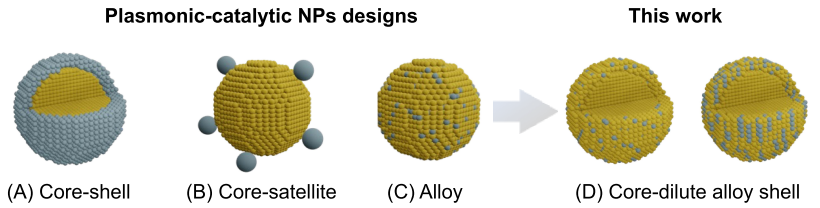

Figure 1. (A–C) Plasmonic-catalytic antenna-reactor NP morphologies: (A) core–shell, (B) core–satellite, and (C) alloyed NPs. The plasmonic and catalytic components are shown in yellow and gray, respectively. (D) NP morphologies developed herein comprise a plasmonic core (Au) and a plasmonic-catalytic alloyed AuPd shell containing low contents of the catalytic metal (Pd, approximately 10 atom %).

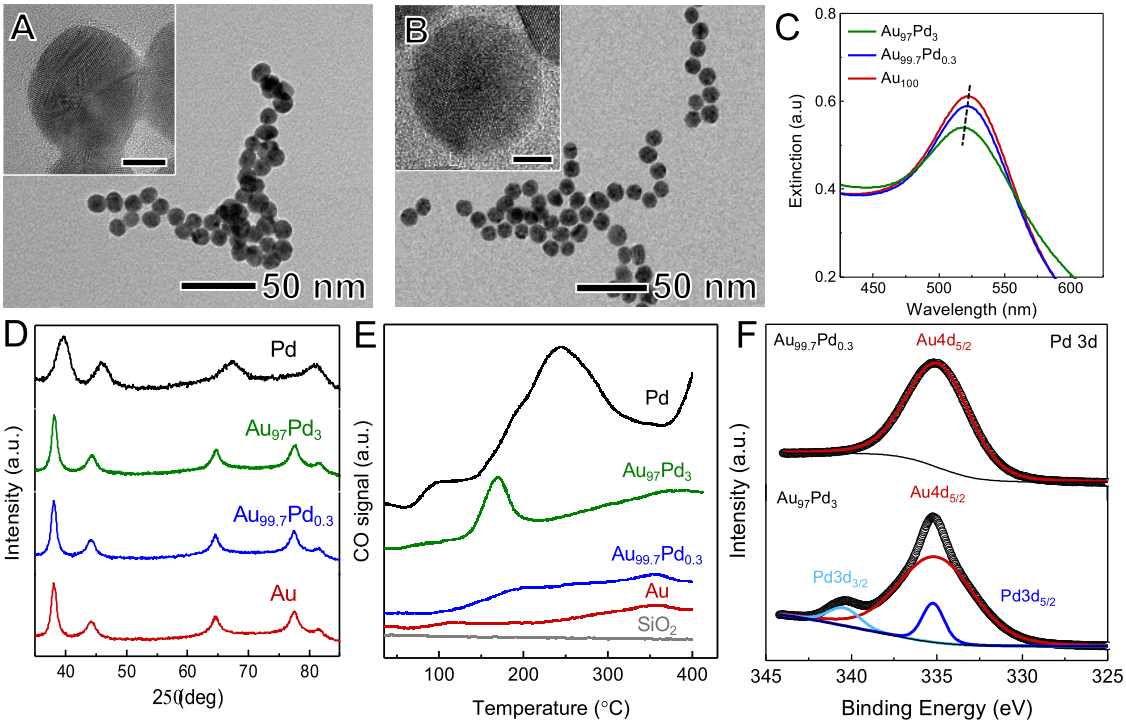

Figure 2. (A, B) TEM images of $Au_{99.7}Pd_{0.3}$ and $Au_{97}Pd_3$ NPs. Scale bars in the insets correspond to 5 nm. (C) UV–vis extinction spectra were recorded from aqueous suspensions containing the $Au_{99.7}Pd_{0.3}$ (blue trace) and $Au_{97}Pd_3$ (green trace) NPs. The spectrum of Au NPs employed as seeds during the synthesis is also shown for comparison (red trace). (D) XRD patterns and (E) CO-TPD for $Au_{99.7}Pd_{0.3}$ (blue trace) and $Au_{97}Pd_3$ (green trace) NPs. The XRD and CO-TPD data for Au and Pd NPs and SiO_2 (CO-TPD only) are also shown for comparison (red and black traces, respectively).

plasmonic-catalytic antenna-reactor NPs.[10−12] In the core−-shell NPs, the plasmonic component is encased within the shell of the catalytic material. This allows for the isolation of the core from reactants while the shell can be tailored to provide the desired catalytic sites. In the core−satellite NPs, the plasmonic core is not isolated, and smaller NPs of the catalytic component (satellites) are deposited around larger NPs of the plasmonic core. In alloys, the plasmonic and catalytic components are mixed through the NPs. These systems have been extensively employed to enable the study and optimization of catalytic properties.[10−12,14,17−20] Nevertheless, they often compromise functionality, as the incorporation of the catalytic component into these designs usually leads to a decrease in the optical properties (thereby decreasing the potential plasmonic enhancement of the catalytic activity).

To overcome these limitations and simultaneously maximize both optical and catalytic properties, we here demonstrate the synthesis of bimetallic Au@AuPd NPs by focusing on the integration of ultralow loadings of catalytically active palladium into the surface of Au NPs. The goal is to achieve NPs with an Au core and a dilute alloyed AuPd shell with low Pd contents (around 10 atom %). This is illustrated in Figure 1D. Due to the high catalytic activity of Pd for certain reactions, this can allow for applications in plasmonic catalysis and solar-driven chemistry, where both optical and catalytic activities can be optimized. By combining experimental investigations and theoretical analyses, we elucidate how this Au@AuPd NP design enables enhanced catalytic activity and selectivity under visible light illumination to enable their utilization in a wide range of catalytic processes.

RESULTS AND DISCUSSION

The Au@AuPd NPs were prepared by a seeded growth approach using Au NPs as seeds, K_2PdCl_4 as a Pd precursor, ascorbic acid as a reducing agent, and water as the solvent at 70 °C. Two samples where the ratio between Au NPs and the Pd precursor was adjusted led to samples denoted $Au_{97}Pd_3$ and $Au_{99.7}Pd_{0.3}$, respectively, based on the microwave plasma atomic emission spectroscopy (MP-AES) elemental analysis (Table S1). Here, a surface alloy containing Au and Pd forms

https://doi.org/10.1021/acsnano.4c07076
ACS Nano 2024, 18, 24391−24403

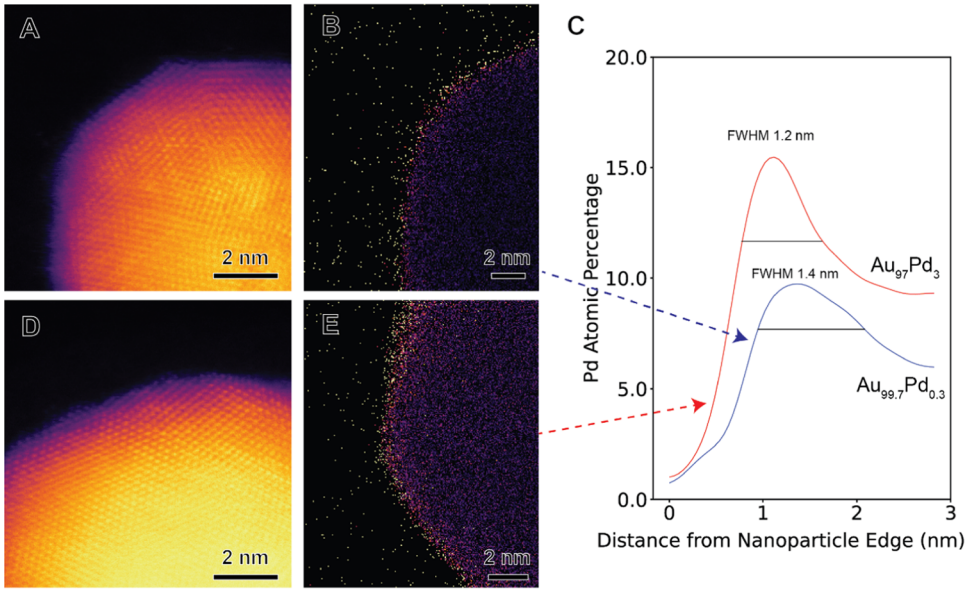

Figure 3. Elemental distributions in $Au_{99.7}Pd_{0.3}$ and $Au_{97}Pd_3$ NPs. (A, D) STEM−HAADF images, (B, E) STEM−EDX elemental maps for Pd in $Au_{99.7}Pd_{0.3}$ (A, B) and $Au_{97}Pd_3$ NPs (D, E). (C) EDX line profiles averaged over pixels certain distances from the NP edges for $Au_{99.7}Pd_{0.3}$ and $Au_{97}Pd_3$ NPs from the NPs in (B) and (E), respectively. The full width at half-maximum (FWHM) of the Pd surface enrichment peak is indicated in (C) for both samples.

when the reduced Pd species interacts with the Au-based surface.

Figure 2A,B shows transmission electron microscopy (TEM) images of $Au_{99.7}Pd_{0.3}$ and $Au_{97}Pd_3$ NPs. The particles are spherical and relatively uniform in size, with diameters of 15.4 ± 1.4 and 16.2 ± 1.7 nm for $Au_{99.7}Pd_{0.3}$ and $Au_{97}Pd_3$, respectively (Figure S1). These diameters are only slightly larger than the original Au seed particles, which had identical morphology and diameters of 14.4 ± 1.7 nm (Figure S2), as expected from the low Pd content in the added shells. The UV−VIS extinction spectra (Figure 2C) from aqueous suspensions of $Au_{97}Pd_3$, $Au_{99.7}Pd_{0.3}$, and Au NPs (green, blue, and red traces, respectively) show that all NPs exhibit extinction bands within the visible spectrum. This is due to the excitation of a dipolar LSPR mode, in which a gradual reduction in the intensity of the band and a slight blue shift is seen when the Pd content in the NPs increases.[21] The LSPR bands are centered at 517, 520, and 522 nm for $Au_{97}Pd_3$, $Au_{99.7}Pd_{0.3}$, and Au NPs, respectively. These variations in intensity and position are consistent with the deposition of Pd on Au and indicate that lower Pd loadings result in more pronounced LSPR bands.[21] The powder X-ray diffraction (XRD) diffraction patterns (Figure 2D) acquired from the $Au_{99.7}Pd_{0.3}$ and $Au_{97}Pd_3$ NPs supported on SiO_2 substrates (blue and green traces, respectively) only show peaks which are assigned to *fcc* Au (the XRD patterns for Au and Pd NP references are also shown as red and black traces, respectively). This agrees with the low Pd content in the samples and shows that no crystalline impurities were present at detectable amounts. The $Au_{99.7}Pd_{0.3}$ and $Au_{97}Pd_3$ NPs have a low Pd content and a core−shell structure with a thin (1.4 and 1.5 nm) alloyed AuPd shell (according to electron microscopy results discussed below). Given the low Pd content in the NPs and the size of the alloyed shell, shifts to higher angles in the XRD peaks of Au due to Pd incorporation are expected to be very subtle. Moreover, due to the core−shell morphology, the dominant diffraction signal still arises from the Au core, which can mask subtle shifts in the shell's diffraction peaks. These observations are in agreement with our results in which a clear slight shift to higher angles due to the presence of Pd was not obvious.

CO temperature-programmed desorption (CO-TPD) was performed to gain insights into the surface properties of the NPs. CO-TPD is an important method to determine CO-metal bond energy in Pd and can be described by including electrostatic interactions and π-back bonding from the Pd to CO.[22,23] Figure 2E shows the CO-TPD profiles for the $Au_{99.7}Pd_{0.3}$ and $Au_{97}Pd_3$ NPs supported on SiO_2 (blue and green traces, respectively). Au and Pd NP references supported on SiO_2 and the uncoated SiO_2 support are also shown as references (red, black, and gray traces, respectively). The CO-TPD profile for Pd NPs displays distinctive peaks at 100 and 250 °C, which can be assigned to weakly and moderately adsorbed CO species, respectively.[22] It has been proposed that weakly adsorbed CO can correspond to CO bound to terrace atop Pd sites, while moderately adsorbed CO is bound to bridge and edge sites of Pd as well as to 3-fold hollow sites.[24,25] For the Au@AuPd NPs, the intensities of the CO desorption features decrease with a decreasing Pd content. In fact, only a broad and weak signal centered at 190 °C is detected for $Au_{99.7}Pd_{0.3}$ NPs (blue trace). For $Au_{97}Pd_3$ NPs, the desorption signal is shifted to 170 °C (relative to 250 °C in Pd). This shift to lower temperatures for $Au_{97}Pd_3$ and $Au_{99.7}Pd_{0.3}$ NPs relative to that of pure Pd agrees with the weakening of the CO adsorption as alloying with Au takes place.[22,24−26] Interestingly, the higher temperature peak for $Au_{99.7}Pd_{0.3}$ compared to $Au_{97}Pd_3$ indicates that the strength of CO adsorption is higher on $Au_{99.7}Pd_{0.3}$ relative to $Au_{97}Pd_3$ NPs. This peak has a lower intensity in $Au_{99.7}Pd_{0.3}$ than in $Au_{97}Pd_3$ NPs due to the lower surface Pd content. It is plausible that the lower Pd concentration in $Au_{99.7}Pd_{0.3}$ leads to differences in the Pd distribution at the surface relative to $Au_{97}Pd_3$, which could cause a stronger interaction with CO adsorbed on the atop sites. The calculated amount of adsorbed CO corresponds to

https://doi.org/10.1021/acsnano.4c07076
ACS Nano 2024, 18, 24391−24403

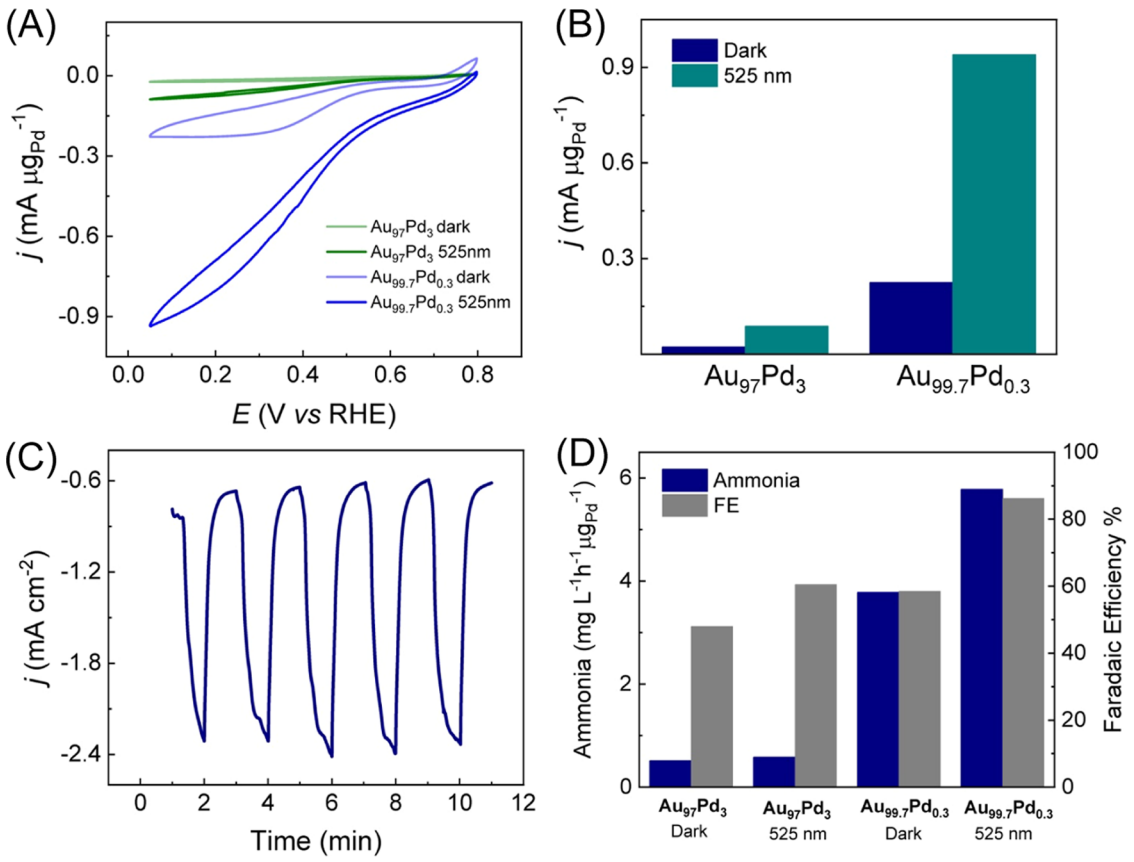

Figure 4. (A) Cyclic voltammograms recorded at 0.010 V s^{-1} for $Au_{97}Pd_3$ (green trace) and $Au_{99.7}Pd_{0.3}$ (blue trace) in the presence of 10 mmol L^{-1} $NaNO_2$ in 0.1 M $HClO_4$. Measurements in the dark (lighter line) and under light irradiation (525 nm, darker line) are shown. (B) Bar graph depicting the current density at 0.05 V for $Au_{99.7}Pd_{0.3}$ and $Au_{97}Pd_3$ under the dark (blue column) and light irradiation (green column) conditions. (C) Chronoamperometric curves for $Au_{99.7}Pd_{0.7}$ NPs were recorded at 0.050 V in 0.1 M $HClO_4$ containing 10 mmol L^{-1} $NaNO_2$ in on/off conditions under 525 nm light irradiation. (D) Ammonia concentration (blue bar) and Faradaic efficiency to/of ammonia production (gray bar) at −0.1 V (RHE) on $Au_{99.7}Pd_{0.3}$ and $Au_{97}Pd_3$ NPs in the dark and under 525 nm light irradiation conditions.

0.731 and 0.199 μmol/g_{cat} for $Au_{97}Pd_3$ and $Au_{99.7}Pd_{0.3}$ NPs, respectively. It is important to note that CO does not adsorb on Au or SiO_2 under our conditions, as illustrated by the absence of any signals in the CO-TPD profiles for Au and SiO_2.

The X-ray photoelectron spectroscopy (XPS) spectra for the Au 4f core level for $Au_{97}Pd_3$ and $Au_{99.7}Pd_{0.3}$ NPs are shown in Figure S3. Two peaks at 88.0 and 84.0 eV, assigned to the Au $4f_{7/2}$ and $4f_{5/2}$ doublets of Au^0, were detected for both samples.[27] No shifts in the Au peaks were detected when the Pd content was varied, which can be attributed to the low Pd loading in the samples or the absence of detectable electronic interactions between Au and Pd in our samples (the interaction would be expected in an alloy with a higher Pd loading). Figure 2F shows the XPS spectra for $Au_{97}Pd_3$ and $Au_{99.7}Pd_{0.3}$ NPs in the Pd 3d core-level region. Usually, Pd^0 is characterized by the presence of a doublet with peaks at 335 and 340 eV assigned to $3d_{5/2}$ and $3d_{3/2}$, respectively.[28] These signals can be identified in the $Au_{97}Pd_3$ NPs (bottom trace). Our data also shows that the Pd $3d_{5/2}$ signal overlaps with and is expected to be overshadowed by the Au $4d_{5/2}$ peak at 335 eV because of the low Pd content in this sample.[29] Thus, the Pd $3d_{3/2}$ peak more clearly shows the presence of Pd. From the $Au_{99.7}Pd_{0.3}$ sample, no detectable Pd signals were observed because of the low Pd content.

Figure 3A−F shows high-angle annular dark field (HAADF) scanning transmission electron microscope (STEM) images, STEM energy-dispersive X-ray fluorescence (STEM−EDX) elemental maps, and EDX elemental line scans for $Au_{99.7}Pd_{0.3}$ and $Au_{97}Pd_3$ NPs. The imaging at atomic resolution of both $Au_{99.7}Pd_{0.3}$ and $Au_{97}Pd_3$ NPs (Figure 3A,D, respectively) indicates that Pd is not present as protruding surface islands, but the NPs have relatively smooth surfaces. STEM-EDX analysis shows the distribution of Pd at the surface of the NPs for both $Au_{99.7}Pd_{0.3}$ and $Au_{97}Pd_3$ (as depicted in Figure 3B,E, respectively). The HAADF STEM intensity line scans show a smoothly decaying surface profile, consistent with the alloying of Au and Pd at the surface rather than a pure Pd shell (Figure S4). This is also supported by the STEM-EDX line scans (Figure S9) that show the Au signal persisting to the edge of the nanoparticle in both cases. Extracting averaged elemental profiles based on the distance of pixels from NP edges reveals similar Pd-rich AuPd shell thicknesses of 1.4 nm for $Au_{99.7}Pd_{0.3}$ and 1.2 nm for $Au_{97}Pd_3$ (Figure 3C), corresponding to a thickness of ∼4 and ∼5 atomic layers, respectively. The elemental quantification of STEM-EDX is challenging for the low alloying contents but was achieved by Python-based fitting using all of the available X-ray peaks for each element (see the Supporting Information for full details). Analysis of the summed STEM-EDX spectra for multiple NPs (as depicted in Figure S5) provided mean compositions of 92.7 atom % Au

https://doi.org/10.1021/acsnano.4c07076
ACS Nano 2024, 18, 24391−24403

and 7.2 atom % Pd for $Au_{97}Pd_3$ NPs, and 96.3 atom % Au and 3.7 atom % Pd for $Au_{99.7}Pt_{0.3}$ NPs with standard deviation errors of 0.5 and 0.4 atom % (Figures S6 and S7). However, as Pd was only found to be present within the shell region, a better estimate of the NP elemental content is achieved by assuming a core@shell NP morphology with the shell thickness given by the full width at half-maximum (FWHM) of the measured Pd enrichment at the surface (see Figure S8). This allows estimation of the AuPd shell compositions as 25.3 atom % Pd and 10.2 atom % Pd for $Au_{97}Pd_3$ and $Au_{99.7}Pd_{0.3}$, respectively. These results indicate the formation of a Au core and a AuPd alloyed shell in both the $Au_{99.7}Pd_{0.3}$ and $Au_{97}Pd_3$ NPs, where the concentration of Pd in the alloyed shells decreases as the loading of Pd in the NPs decreases.

We then investigated how the Au@AuPd core@shell morphology, the different compositions of the shells, and the LSPR excitation in the visible range influence the electrocatalytic activities of the $Au_{99.7}Pd_{0.3}$ and $Au_{97}Pd_3$ NPs. We employed nitrite (NO_2^- reduction reaction (NO_2RR)) as a model transformation (as shown in Figure 4). The cyclic voltammograms obtained in the presence of NO_2^- exhibited characteristic features of the reduction of NO_x compounds (Figures 4A and S10, respectively).[30] Voltammograms obtained for Au NPs in the presence of NO_2^- and for $Au_{99.7}Pd_{0.3}$ and $Au_{97}Pd_3$ NPs under blank conditions (in the absence of NO_2^-) can be found in Figure S11, showing that the samples have negligible (photo)electrochemical activity under these conditions. The current densities for both $Au_{99.7}Pd_{0.3}$ and $Au_{97}Pd_3$ samples increased under visible light illumination because of the LSPR-enhanced NO_2RR. Figure 4A shows cyclic voltammograms where the current densities are normalized by the mass of Pd to better compare the performance of the samples, as Pd is the only electrocatalytically active species under our employed conditions. These indicate that the current densities for the reduction of NOx compounds are higher both in the dark and under light illumination conditions for the $Au_{99.7}Pd_{0.3}$ NPs compared to those of $Au_{97}Pd_3$. The calculated mass activities at 0.05 V are depicted in Figure 4B. For both $Au_{99.7}Pd_{0.3}$ and $Au_{97}Pd_3$ NPs, activities increased under plasmonic excitation relative to those under dark conditions. Specifically, a 4-fold increase was detected in both samples (from −0.23 to −0.94 mA μg_{Pd}^{-1} in $Au_{99.7}Pd_{0.3}$ and from −0.023 to −0.089 mA μg_{Pd}^{-1} in $Au_{97}Pd_3$). It can also be observed that $Au_{99.7}Pd_{0.3}$ NPs displayed higher activities compared to $Au_{97}Pd_3$ under both dark and light irradiation conditions. Specifically, 10-fold and 10.6-fold increases in mass activity were detected in the dark and light illumination conditions, respectively. This indicates that the more dilute Pd distribution and lower Pd content in the $Au_{99.7}Pd_{0.3}$ surface-alloyed shell were important for the increased catalytic activity even without LSPR excitation.

Under dark conditions, the plasmonic effects are absent, and the catalytic activity primarily depends on the intrinsic properties of the Pd within the AuPd shell. For both Pd concentrations investigated in this study, the thickness of the alloyed surface AuPd shell is similar, and the difference relies mainly on the Pd concentration, which leads to Pd being more dilute in terms of its distribution in the shell having a lower Pd content. This more dilute distribution enhances the interaction between Pd sites and the reactants involved in the NO_2RR, promoting selective adsorption and activation of intermediates crucial for the formation of NH_3. In contrast, a higher Pd loading can lead to the formation of more Pd-rich regions, which may exhibit different electronic properties and potentially introduce competing pathways or side reactions that reduce selectivity toward NH_3. Furthermore, the electronic interaction between Au and Pd in the dilute alloy plays a significant role, as also corroborated by our DFT calculations (discussed later in the text). The alloying effect at low Pd content can modify the electronic structure of Pd, making it more effective for the NO_2RR even without plasmonic enhancement by enhancing the binding and activation of nitrogen-containing intermediates, leading to a higher yield of NH_3. Under plasmonic excitation, the increase in catalytic activity for the $Au_{99.7}Pd_{0.3}$ sample can also be related to the higher light absorption enabled by the lower Pd content. The on−off transients for $Au_{99.7}Pd_{0.3}$ NPs under chopped light excitation at 525 nm (Figure 4C) show fast and reproducible current responses to the on−off illumination cycles in agreement with the NO_2RR plasmonic enhancement during/under light illumination conditions via hot charges and localized heating.[31]

Next, we investigated how the compositional features of the NPs and plasmonic effects influence the reaction selectivity toward the formation of NH_3. As shown in Figure S12, the NO_2RR can lead to a variety of products, including NO, N_2, N_2O, N_2OH, and NH_3. Under acidic conditions employed herein, it is reported that NO_2^- can be easily converted into $NO_{(ad)}$ at the surface of the catalyst, which represents the key intermediate for the NO_2RR.[32] In order to evaluate the reaction selectivity under dark and light conditions, we quantified the amount of NH_3 produced by the indophenol method (Figure S13).[33] Figure 4D shows the concentrations of NH_3 produced (blue bars) under dark and light irradiation conditions for $Au_{99.7}Pd_{0.3}$ and $Au_{97}Pd_3$ NPs together with the respective Faradaic efficiency percentages (FE, gray bars). The amount of NH_3, and thus the selectivity toward NH_3, was significantly higher for the $Au_{99.7}Pd_{0.3}$ relative to $Au_{97}Pd_3$. Moreover, with $Au_{99.7}Pd_{0.3}$, a significant increase in selectivity was detected under the light irradiation conditions, showing that the plasmonic excitation not only increases reaction rates (catalytic activity) but also enables control over reaction selectivity. The detected NH_3 concentrations after 1 h of electrolysis at 0.05 V for $Au_{97}Pd_3$ NPs were 0.5 and 0.6 mg L^{-1} h^{-1} μg_{Pd}^{-1} under dark and light excitation conditions, respectively. This corresponded to FE values of 48 and 61%, respectively. On the other hand, the NH_3 concentration was 3.8 and 5.8 mg L^{-1} h^{-1} μg_{Pd}^{-1} under the dark and light excitation conditions, respectively, for the $Au_{99.7}Pd_{0.3}$ NPs. This corresponds to an increase of 7.6 and 9.7-fold for the light and dark conditions, respectively, relative to those of the $Au_{97}Pd_3$ NPs, and a significant enhancement in selectivity for the formation of the desirable NH_3 due to the plasmonic excitation. The FEs were also improved for $Au_{99.7}Pd_{0.3}$ relative to $Au_{97}Pd_3$ to 58.5 and 86.2% under dark and light excitation conditions, respectively.

Upon light absorption, the excitation of localized surface plasmon resonance (LSPR) leads to strong electric field enhancements (E/E_0) near the surfaces of plasmonic NPs.[1] Figure S14 shows DDA simulations on the magnitudes and special distribution of the electric field enhancements for $Au_{99.7}Pd_{0.3}$ and $Au_{97}Pd_3$ NPs excited at 525 nm. It can be observed that both NPs display similar electric field enhancements, and the fields are strongly concentrated along the polarization direction of the incoming electromagnetic wave. The LSPR excitation primarily undergoes nonradiative Landau

https://doi.org/10.1021/acsnano.4c07076
ACS Nano 2024, 18, 24391−24403

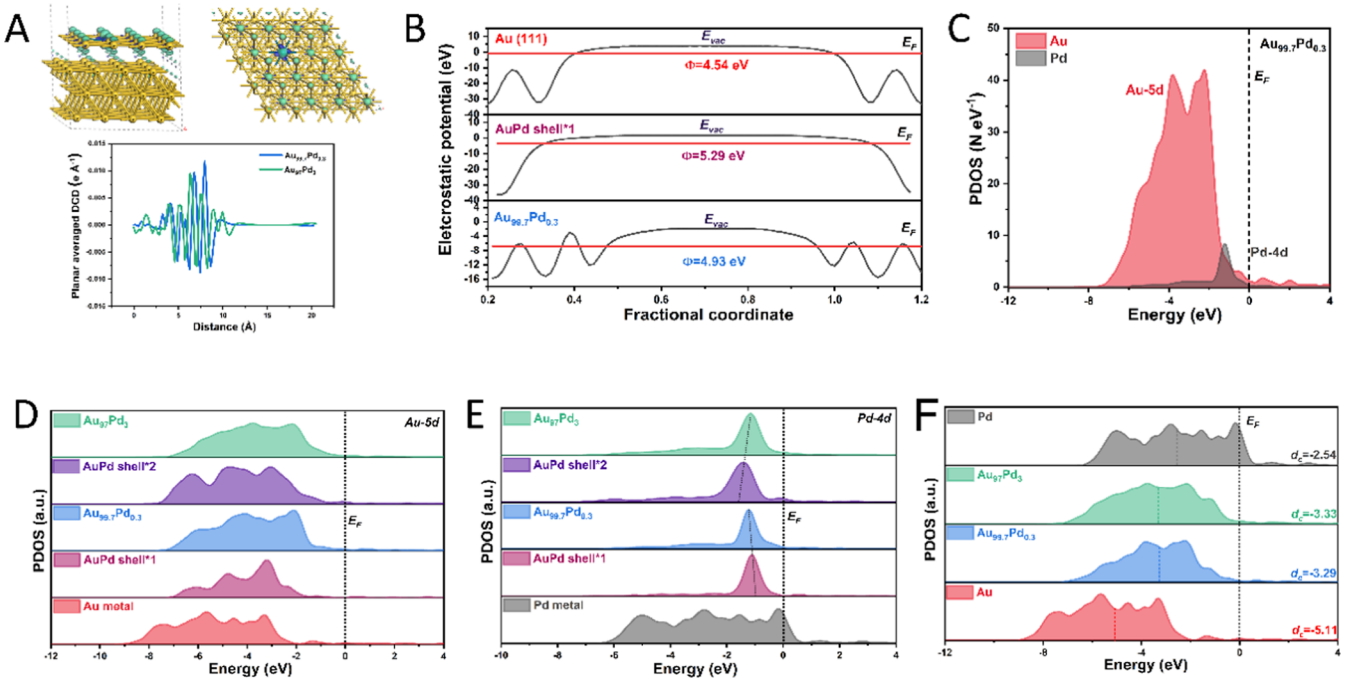

Figure 5. (A) Charge density differences in the constructed $Au_{99.7}Pd_{0.3}$ NP model (side and top views) and the plane-averaged differential charge density (DCD) across the interface (bottom panel). The blue and bright green contours represent the regions of electron accumulation and depletion, respectively. (B) Electrostatic potentials for Au (111), AuPd alloy shell, and $Au_{99.7}Pd_{0.3}$ models. (C) Projected density of state (PDOS) curves for $Au_{99.7}Pd_{0.3}$ model NPs. PDOS of (D) Au-5d and (E) Pd-4d within different coordination environments. (F) d-PDOS on Au, $Au_{99.7}Pd_{0.3}$, $Au_{97}Pd_3$, and Pd models. Shell*1 and shell*2 refer to the AuPd alloy shell in $Au_{99.7}Pd_{0.3}$ and $Au_{97}Pd_3$ NPs, respectively.

damping to produce energetic charge carriers that quickly redistribute their energy, generating hot electrons and hot holes with a quasi-Fermi−Dirac distribution.[34,35] These electron−hole pairs further relax by transferring energy to the phonon modes of the metal nanoparticles, resulting in localized heating effects.

In terms of increasing reaction rates, both energetic hot carriers and localized heating induced by LSPR can contribute to plasmonic catalysis.[36,37] However, the untangling of the effect of localized heating and hot charge carriers over activities remains challenging.[4,38] In plasmonic electrocatalysis, it has been reported that the local temperature at the electrocatalyst/medium interface under laser irradiation from 0 to 2.55 W/cm^2 (more intense than our LED source) was only moderately higher than that under dark conditions and that the temperature increase resulting from photothermal heating has low influence on the HER performances.[31] Also, we tried to mitigate the heat effects herein by performing all of the experiments in a temperature-controlled system. Figure S15 suggests a mechanism for the enhanced NO_2RR performances under light illumination based on the generation of LSPR-excited charge carriers. LSPR excitation leads to the generation of hot carriers from the Au plasmonic core. The hot electrons generated by the Au NPs can transfer to the AuPd shells, where they participate in enhancing reaction rates by activating surface adsorbates.[39,40] The holes are transported to the counter electrode with the assistance of an external voltage. This activation mechanism is supported by the detected linear dependence of current density with light intensity (Figure S16).[38,41]

Beyond increasing reaction rates, plasmonic excitation also leads to a control over reaction selectivity.[7,42,43] This can be achieved through several pathways, including plasmon-mediated selective adsorption, plasmon-mediated selective activation, and plasmon-mediated selective desorption.[43] In plasmon-mediated selective adsorption, the electromagnetic field due to the LSPR can add an optical force to selectively concentrate polar molecules on the catalyst surface and change the adsorption energy.[43] When several kinds of reactants with different functional groups are involved in reactions, the molecules with larger dipole moments tend to be concentrated near the plasmonic catalyst with the assistance of a local electromagnetic field, resulting in the preferential adsorption and activation of such molecules. In plasmon-mediated selective activation, LSPR-excited charge carriers generated by plasmonic excitation can selectively populate specific electronic states of adsorbed molecules, favoring certain reaction pathways over others.[44,45] For example, the injection of hot electrons into the antibonding molecular orbitals enables a reduced bond order, making the breakage of chemical bonds easier. Due to the LSPR, the energy of highly energetic hot electrons can be tailored to allow for their specific injection into particular adsorbate orbitals. Such adsorbates are thus activated and converted preferentially. Finally, in terms of plasmon-mediated selective desorption, the desorption of intermediates and products is sometimes the rate-limiting step of chemical reactions. In plasmonic catalysis, hot carrier injection to adsorbates may lead to the vibrational excitation of adsorbates, which weakens the metal−adsorbate interaction and promotes the desorption of adsorbates from the catalyst surface, which alters the surface coverage of intermediate species, which potentially results in a modified reaction pathway.[10,42]

https://doi.org/10.1021/acsnano.4c07076
ACS Nano 2024, 18, 24391−24403

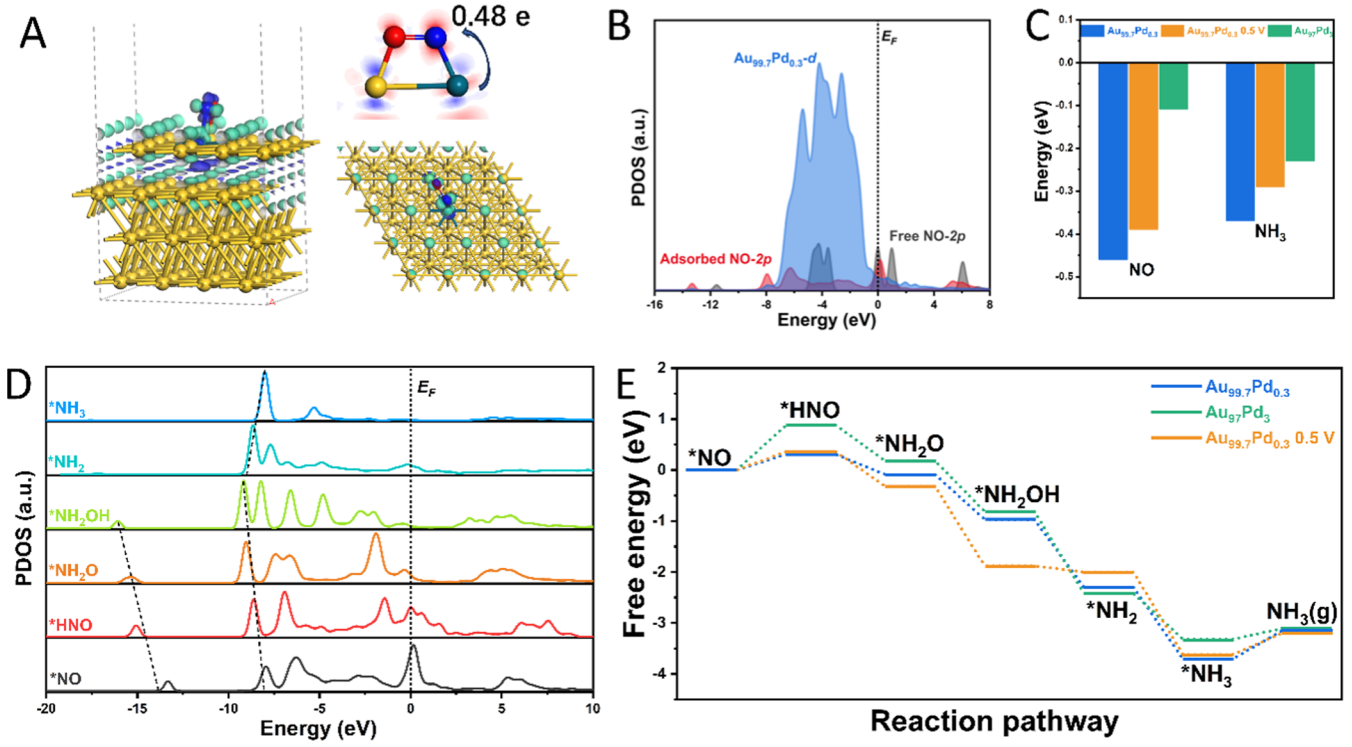

Figure 6. (A) Charge density differences and Mulliken charge analysis in the constructed $Au_{99.7}Pd_{0.3}$ NP model containing a NO molecule adsorbed at the proposed surface sites. The blue and bright green contours represent the regions of electron accumulation and depletion, respectively. For two-dimensional (2D) maps, the scale from blue to red is −0.4 to 0.4 e. (B) PDOS for a free (gray) and absorbed (red) NO molecule (2p levels) at the surface site in the $Au_{99.7}Pd_{0.3}$ NP model. (C) Adsorption energies of NO and NH_3 on $Au_{99.7}Pd_{0.3}$ (with/without applied voltage) and $Au_{97}Pd_3$ (111) model NP surfaces. (D) PDOS of key intermediates in $Au_{99.7}Pd_{0.3}$ NP model during the reaction progress. (E) Free energy profiles for the reaction pathway on $Au_{99.7}Pd_{0.3}$ (with/without applied voltage) and $Au_{97}Pd_3$ models.

It is important to note that it has been reported that Pd NPs can display LSPR excitation in the visible range via control of size (when NPs are above 50 nm) or shape (cubes, cages, flowers, stars, and plates, for example).[46] However, below 20 nm, spherical Pd NPs display an LSPR in the UV region. Therefore, in our $Au_{99.7}Pd_{0.3}$ and $Au_{97}Pd_3$ NPs, it is expected that the LSPR excitation from Pd plays no significant role in the detected plasmonic-catalytic activities.

We performed density functional theory (DFT) calculations to gain a further understanding of the observed catalytic activity and selectivity enhancement. The theoretical models used to understand the electronic structure of the $Au_{99.7}Pd_{0.3}$ and $Au_{97}Pd_3$ NPs are depicted in Figure S17. Charge density difference (CDD, Figure 5A) and Mulliken charge (Figure S18 and Table S2) analyses show the electron-rich nature of the Pd site and the local charge redistribution at the surface. In addition, electron localization was evaluated by electron local function (ELF) to show the bond characteristics and charge transfer between Pd and the surrounding Au atoms.[47] As shown in Figure S19, the ELF value around the Pd atom in the $Au_{99.7}Pd_{0.3}$ model was lower than that around the Au atoms, indicating that the electrons surrounding the Pd atom are more delocalized.[48] The observed local charge redistribution and charge density regions around the isolated Pd atoms at the surface in the $Au_{99.7}Pd_{0.3}$ model may be responsible for favoring the migration of the LSPR-induced hot charges to the Pd sites under the light irradiation, leading to the higher reaction rates. As for the $Au_{97}Pd_3$ NPs, the larger number of Pd atoms means that the local charge distribution mainly occurs at the Au-AuPd interface, not on the surface (Figure S20). The planar average charge density differences (Figure 5A, bottom panel) show the formation of an internal electric field within the core−shell structure for both $Au_{99.7}Pd_{0.3}$ and $Au_{97}Pd_3$ NP models. This is also supported by the calculated work functions (WF) of pure Au, the AuPd shell, and $Au_{99.7}Pd_{0.3}$ (Figure 5B). Due to the difference in the WF values between pure Au (4.54 eV) and the AuPd shell (5.29 eV), the contact between the Au core and the AuPd shell could cause charge redistribution across the interface, enabling electron transfer from Au to AuPd until their work functions become equivalent/aligned (for $Au_{99.7}Pd_{0.3}$, WF is 4.93 eV).[49] Therefore, under the light excitation conditions, LSPR-excited hot electrons would spontaneously migrate to the AuPd shell, while holes are transferred to the counter electrode, contributing to the enhanced performance under the LSPR excitation by boosting separation of the photon-generated carriers.[50]

The projected partial density of states (PDOS) shown in Figure 5C indicates that the Pd-4d orbital is located close to the Femi level (E_F, band center at −1.56 eV), while the Au-5d orbital is buried at a deeper position away from E_F (band center at −3.48 eV). This supports the assertion that Pd acts as the main active site for the catalytic reaction due to the stronger interaction with adsorbed NO molecules (Figure 6B) and that, under the LSPR excitation conditions, hot electrons transferred to the Pd sites can contribute to the accelerated reaction rates.[51] The site-dependent PDOS of the Au-5d bands was also calculated (Figure S21). From the bulk to the Au-AuPd interface and then into the AuPd shell (from bottom to top in Figure S21), the Au-5d PDOS exhibited a trend toward lower energy (further to the Fermi energy). For a more in-

https://doi.org/10.1021/acsnano.4c07076
ACS Nano 2024, 18, 24391−24403

depth understanding of the electronic structures, we compared the electronic structures of Au-5d and Pd-4d orbitals in different environments (Figure 5D,E). For $Au_{99.7}Pd_{0.3}$ and $Au_{97}Pd_3$ models, both the Au-5d bands exhibited an upshifting trend compared with those of pure Au metal and individual shells consisting of AuPd alloys. This indicates an improved electroactivity and effective d−d orbital coupling within the obtained core−shell structure relative to those of the pure metals or alloy counterparts. On the other hand, both $Au_{99.7}Pd_{0.3}$ and $Au_{97}Pd_3$ displayed more positive positions of the overall Pd-4d band relative to the d-band center of the Pd metal (Figure 5E). However, the Pd-4d band in $Au_{99.7}Pd_{0.3}$ was negatively shifted compared with that in the AuPd shell (shell*1), which is contrary to the $Au_{97}Pd_3$ behavior. This might be caused by the lower concentration of Pd, which can optimize the binding strengths between Pd active sites and intermediates.[52] This is consistent with our results from CO-TPD. The overall electronic structure comparison with the pure Au metal also indicated that the overall d-band centers (d_c) have an increased density of states after the introduction of the AuPd alloy shell (Figure 5F). This leads to more adsorbate antibonding states being pulled above the E_F and enhancing the electron transfer between the adsorbate and active sites.[53] Therefore, these results support our experimental findings on the improved electrocatalytic activity for $Au_{99.7}Pd_{0.3}$ NPs relative to that of $Au_{97}Pd_3$ under dark and light irradiation conditions.

Figure S22 shows the calculated reaction pathway for the reduction of NO to NH_3. Figure 6A shows the optimized configuration for a NO molecule adsorbed on Pd sites on the $Au_{99.7}Pd_{0.3}$ surface. The calculated CDD results suggest that NO adsorption on the $Au_{99.7}Pd_{0.3}$ surface results in a stronger local charge redistribution over the active sites than that on the $Au_{97}Pd_3$ surface (Figure S23), causing more electron migration from the surface to the adsorbed *NO species (supported by quantitative Mulliken charge analysis). The PDOS for adsorbed (*NO) and free NO is shown in Figure 6B and reveals the strong interaction at the surface with the downshift of 2p orbitals upon adsorption.[54] To quantitatively evaluate the interaction between different Pd sites ($Au_{99.7}Pd_{0.3}$ and $Au_{97}Pd_3$ NPs) and *NO, the projected crystal orbital Hamilton population (pCOHP) of the Pd−N bond (Pd in the surface site and *N, Figure S24) was calculated. The integral COHP value (ICOHP) could be calculated by integrating the partial COHP below the E_F, suggesting the number of bonded electrons between the selected Pd and N atoms and the corresponding bonding strength.[55] It is notable that the ICOHP of Pd−N in $Au_{99.7}Pd_{0.3}$ is larger than that of $Au_{97}Pd_3$ and demonstrates a stronger NO adsorption (Figure S25). The calculated adsorption energies of NO (Figure 6C) agree with these results, suggesting that control over the composition of Pd in the AuPd shells modulates the adsorption strength of NO at the surface.

The PDOS analysis of NO, the reaction intermediates, and NH_3 at the $Au_{99.7}Pd_{0.3}$ NP surface were calculated (as shown in Figure 6D). With the progress of the hydrogenation reaction, the conversion of *NO to *NH_3 exhibits two linear-like trends, which might be ascribed to (N−O)σ and (N−H)σ binding energies.[51] These two linear trends for (N−O)σ and (N−H)σ indicate the substantial efficiency of p−d electron transfer during the NO_2RR on the $Au_{99.7}Pd_{0.3}$ NPs. The energy profiles for the NO_2RR are shown in Figure 6E. For $Au_{97}Pd_3$ NPs, the first step (protonation of *NO to *NHO) is identified as the rate-determining step (RDS) and exhibits a large energy barrier of 0.88 eV, which is consistent with the adsorption energy results (Figure 6C). On the other hand, the energy barrier is reduced to 0.31 eV on $Au_{99.7}Pd_{0.3}$ NPs due to the optimized electronic properties as a result of the change in surface composition, as described herein. Finally, we performed calculations on the superficial charge distribution of the $Au_{99.7}Pd_{0.3}$ NP model in the presence of an applied electric field (0.5 V $Å^{-1}$) to simulate the effect of the LSPR excitation. As shown in Figure S26 and Table S3, the charge distribution at the top surface was altered, and the adsorption energies of NO and NH_3 were affected (Figure 6C, a slight decrease relative to no applied electric field).

Our results indicate that a more dilute concentration of Pd in the shells can contribute to light adsorption, facilitating the transfer of hot carriers to the Pd sites. This effect can lead to enhanced catalytic activity and increased selectivity toward NH_3 formation under light excitation, which is an indicator of a larger extent of reduction of NO_2^- than other products. Furthermore, a more dilute concentration of Pd could promote the hydrogenation pathway while decreasing the formation of N_2, which requires the coupling between two adjacent N-containing species.

CONCLUSIONS

We have developed herein antenna-reactor plasmonic nanoparticles (NPs) composed of a plasmonic Au core and a bimetallic, alloyed plasmonic-catalytic AuPd shell (Au@AuPd). These NPs possess low Pd content that provides the ideal conditions to marry the advantages of strong plasmonic properties, attributed to the LSPR excitation from the Au cores, with enhanced utilization of catalytic metal (the Pd loading corresponded to 3 or 0.3 atom %). Our spectroscopic and electron microscopy investigations showed that by controlling the Pd content in these samples, similar shell thicknesses for the alloys at the Au surface were detected (4 or 5 atomic layers in $Au_{99.7}Pd_{0.3}$ and $Au_{99}Pd_3$ NPs, respectively). As the Pd content decreases, the Pd distribution within the alloyed shells becomes more dilute. This precise manipulation of the Pd distribution enabled optimization of the catalytic activity and increased reaction selectivity under both dark and visible light irradiation conditions due to plasmonic effects. By employing the production of NH_3 from NO_2^- (nitrite reduction reaction, NO2RR) as a model transformation, an increase of 10-fold and 11-fold in mass activity was detected in the dark and light illumination conditions, respectively, for $Au_{99.7}Pd_{0.3}$ relative to $Au_{97}Pd_3$ NPs. CO-TPD and DFT results showed that this optimization of the Pd distribution in $Au_{99.7}Pd_{0.3}$ enabled stronger interactions with adsorbed NO and decreased energy barriers for the NO2RR. Moreover, the presence of pronounced electron accumulation regions at the Pd sites in $Au_{99.7}Pd_{0.3}$ facilitates the effective transfer of LSPR-excited hot electrons to the Pd sites, contributing to the plasmonic enhancements in the NO2RR. The tuning over Pd concentration in the surface AuPd alloys and the plasmonic effect in $Au_{99.7}Pd_{0.3}$ also enabled control over reaction selectivity, with an increase in the formation of NH_3 both in the dark and under light excitation conditions relative to that of $Au_{97}Pd_3$. From $Au_{99}Pd_3$ to $Au_{99.7}Pd_{0.3}$, the reaction selectivity toward the formation of NH_3 under light excitation increased from 3.8 to 5.8 mg $L^{-1}h^{-1}$. This increase in reaction selectivity can be assigned to the larger extent of hydrogenation enabled by the more dilute Pd distribution in the shells of

https://doi.org/10.1021/acsnano.4c07076
ACS Nano 2024, 18, 24391−24403

$Au_{99.7}Pd_{0.3}$ while suppressing the pathway that leads to N_2 (which requires coupling between two adjacent surface N-containing species). We believe that the results presented herein can provide important insights into the rational design of antenna-reactor plasmonic-catalytic NPs with improved activities and selectivity for molecular transformations related to sustainability, which is crucial to achieving the world's net zero goals.

METHODS

Materials and Instrumentation. Chloroauric acid trihydrate ($HAuCl_4 \cdot 3H_2O$, 99.9%, Sigma-Aldrich), potassium hexachloropalladate (IV) (K_2PtCl_6, 99.99%, Sigma-Aldrich), trisodium citrate dihydrate ($C_6H_5Na_3O_7 \cdot 2H_2O$, 99%, Sigma-Aldrich), L-ascorbic acid ($C_6H_8O_6$, 99%, Sigma-Aldrich), nitric acid (HNO_3, 65.0−67.0%, Sigma−Aldrich), silica nanopowder (SiO_2, Sigma-Aldrich), isopropanol (C_3H_8O, HPLC grade 99.9%, Sigma−Aldrich), Vulcan XC-72R (FullCellStore), perchloric acid ($HClO_4$, ACS reagent, 70%, Sigma−Aldrich), and sodium nitrite ($NaNO_3$, trace metals basis 99.999%, Sigma-Aldrich) were used as received. Deionized water (18.2 MΩ•cm Milli-Q system) was used for synthesis and support electrolyte preparation.

Transmission electron microscopy (TEM) images were acquired on a Jeol JEM-1400 TEM. TEM samples were prepared by dispersing the nanoparticle suspension in deionized (DI) water with an ultrasonic bath and drop casting onto carbon-coated copper grids. The histogram of the particle size distribution was determined by individually measuring the diameters of 250 nanoparticles. The suspension containing the NPs was drop cast onto an oxidized Si wafer and dried under ambient conditions before imaging. UV−vis spectra were acquired directly from the NP aqueous suspensions using a Shimadzu UV-2600 spectrometer from 800 to 200 nm with a step size of 1 nm.

Powder X-ray diffraction (PXRD) data of silica-supported NPs was collected on a Bruker D8 Advance in Bragg−Brentano geometry using Cu Kα radiation (λ = 1.5406 Å) with a Ni filter. Diffraction data were collected over a range of 10−70° 2θ (step width 0.02° 2θ, count time 1 s/step). The diffraction patterns have been indexed by comparison with the Joint Committee on Powder Diffraction Standard (JCPDS) files. The elemental composition analysis was performed by Microwave Plasma Atomic Emission Spectroscopy (MP-AES) using Agilent Technologies 4100 MP-AES. Three independent measurements were performed for each sample.

X-ray photoelectron spectroscopy (XPS) was performed using a PREVAC spectrometer with a monochromatized Al Kα anode (1486.7 eV) under an ultrahigh vacuum (10^{-10} mbar). The samples were prepared by drop casting the corresponding suspension containing the NPs onto Si support, followed by drying under ambient conditions. The survey spectra were measured with 200 eV pass energy, and high-resolution spectra were measured with 100 eV pass energy. Casa XPS software was used for data interpretation, and the Shirley background method was employed in the deconvolution process. Some X-ray photoelectron spectra were recorded with a lab-based spectrometer (SPECS GmbH, Berlin) using a monochromated Al Kα source ($h\nu$ = 1486.6 eV) operated at 50 W as the excitation source. In the spectrometer, the X-rays are focused with a μ-FOCUS 600 monochromator onto a 300 μm^2 spot on the sample, and the data are recorded with a PHOIBOS 150 NAP 1D-DLD analyzer in fixed analyzer transmission (FAT) mode. The pass energy was set to 40 eV for survey scans and 20 eV for high-resolution regions. Charge compensation was required for data collection. Recorded spectra were additionally calibrated against the C 1s internal reference. Data interpretation was performed via Casa XPS. A Shirley or two-point linear background was used depending on the spectrum shape.

Temperature-programmed desorption measurements were performed with a Micromeritics 3Flex 3500 instrument. Before analysis, 50−150 mg of the sample was packed into a quartz U-tube reactor and outgassed in a flow of helium (He) at 100 °C for 30 min. Samples were hydrogenated in a flow of H_2 (100 °C for 60 min) to achieve a comparable state of reduction prior to measurement. After hydrogenation, the temperature was set to 35 °C under He flow (100 mL/min). At 35 °C, the flow rate was increased to 200 mL/min, and CO adsorption was started with loop injection. The sample CO saturation was monitored with a thermal conductivity detector (TCD), where at least three injections were performed to achieve full saturation. After CO adsorption, the sample was kept in a He flow (200 mL/min) for 30 min before starting temperature-programmed desorption (35 to 400 °C with a ramp rate of 10 °C/min). Desorbed CO was measured with a mass spectrometer (Balzers Omnistar GSD 300 O3) monitoring CO at 28 m/z.

The high-angle annular dark field (HAADF) scanning transmission electron microscopy (STEM) imaging was performed using a probe-corrected FEI Titan G2 80−200 S/TEM instrument equipped with the Super-X energy-dispersive X-ray fluorescence (EDX) detector and a Gatan Quantum ER imaging filter (GIF) for electron energy loss spectroscopy. The Titan STEM was operated at an accelerating voltage of 200 kV. The HAADF STEM images were acquired using a probe current of 300 pA, convergence semiangle of 21.5 mrad, and a HAADF inner collection angle of 43 mrad. The images were collected with a dwell time of 10 μs, resulting in a total frame time per image of ∼12.6 s. The STEM-EDX spectrum images were collected with a probe current of 300 pA using all 4 EDX detectors for a total acquisition time of ∼10 min. Analysis of the STEM-EDX data was carried out using in-house built Python scripts with packages including Hyperspy v1.6.31.[56]

Model Fitting for EDX Quantification. Quantification of EDX data was initially attempted with Gatan Digital Micrograph and Bruker ESPRIT software, but neither achieved consistently reliable results, likely due to the exceptionally low alloy content and overlapping spectral features. These traditional EDX analysis approaches only consider the intensity of an individual X-ray peak in the EDX spectra to quantify the elemental compositions (e.g., Au Kα). However, many elements have several peaks visible in the X-ray spectrum, the consideration of which has the potential to reduce experimental error since all peaks should reflect the concentration of the appropriate element. Quantification based on the intensity of all X-ray peaks improves the confidence in the intensity measurement of a single peak. Including all such peaks maximizes the information content, which is particularly important for noisy data sets or for which the content of a particular element is low. To combine the information on different EDX peaks for the same element, it is necessary to fit a model to the sum of the spectrum image (Figure S5). This was achieved using Python-based fitting, which involves applying a model consisting of a polynomial background function and a series of Gaussian peaks to the spectrum. The model was then used to extract the quantification.

EDX error minimization can be accomplished by reducing the width of the integration windows to isolate the peaks as much as possible. In addition, the background subtraction window was moved outside of the characteristic peak energy range into flat areas on either side of the peaks. The approximation of mean shell thickness was calculated using the overall atomic % of Au and Pd, considering that all of the Pd detected was on the surface of the particle in a homogeneous shell layer with a composition of 100% Pd. The calculated shell thicknesses for $Au_{97}Pd_3$ and $Au_{99.7}Pd_{0.3}$ NPs were 280 pm (0.28 nm) and 120 pm (0.12 nm), respectively (Pd atomic radius = 0.137 nm). Alternatively, we can consider a model where the Pd content is uniformly distributed within the measured radially averaged shell thickness, r_2, for a particle with radius, r, and a 100% Au core (see Figure S8 for the model). The particles in Figure 3B,E (main text) have r_2 = 1.4 and 1.2 nm and r = 10 and 11 nm for the $Au_{99.7}Pd_{0.3}$ and $Au_{97}Pd_3$, respectively, so this perfect two-phase core−shell model gives the shell a composition of 25.3 atom % Pd and 10.2 atom % Pd for $Au_{97}Pd_3$ and $Au_{99.7}Pd_{0.3}$, respectively. However, we note that the distribution of Pd visible in Figures 3 and S6 is not perfectly homogeneous in the shell region, and the morphology is therefore likely better represented by a core−shell structure with the surface shell having a variable Pd enrichment.

https://doi.org/10.1021/acsnano.4c07076
ACS Nano 2024, 18, 24391−24403

Computational Details. DFT calculations were carried out by the DMol^3 module of Materials Studio.[57] The generalized gradient approximation of Perdew−Burke−Ernzerhof exchange−correlation functionals was used to calculate the exchange and correlation energy in this work.[58] Core treatment was adopted as All Electron to conduct the metal relativistic effect, and the double numerical plus polarization function basis set was used. A smearing of 0.01 Ha (1 Ha = 27.21 eV) to the orbital occupation and 1×10^{-5} Ha convergence criterion for self-consistent-field (SCF) calculations were applied. The van der Waals (vdW) interactions were taken into consideration by the Grimme scheme (DFT-D3).[59] The geometry optimization convergence tolerance for energy change, maximum force, and maximum displacement were 1×10^{-5} Ha, 0.004 Ha/Å, and 0.005 Å, respectively. The vacuum spacing in the direction along the Z axis, with respect to the surface, was 20 Å between neighboring slab images, which is sufficient to eliminate the interactions between the slabs. During the geometry optimizations, only the top AuPd alloy layer was relaxed and the bottom Au layers were fixed at the bulk positions.

The free energy (ΔG) calculations for each elementary step were based on the standard hydrogen electrode model,[60] and the change in reaction free energy can be obtained with the equation below:

$$\Delta G = \Delta E + \Delta E_{ZPE} - T\Delta S \quad (1)$$

where ΔE is the total energy difference before and after intermediate adsorbed, and ΔE_{ZPE} and ΔS are the differences of zero-point energy and entropy, respectively.

For the nitrite reduction reaction, the chemical reaction considered can be summarized with the reaction equations below:

$$^*NO + H^+ + e^- \rightarrow ^*NOH \quad (2)$$

$$^*NOH + H^+ + e^- \rightarrow ^*NHOH \quad (3)$$

$$^*NHOH + H^+ + e^- \rightarrow ^*NH_2OH \quad (4)$$

$$^*NH_2OH + H^+ + e^- \rightarrow ^*NH_2 + H_2O \quad (5)$$

$$^*NH_2 + H^+ + e^- \rightarrow ^*NH_3 \quad (6)$$

$$^*NH_3 \rightarrow ^* + NH_3 \quad (7)$$

where * represents the active site. The zero-point energy and entropy of free molecules and adsorbents were obtained from vibrational frequency calculations.

Synthesis of Au and AuPd NPs. For the synthesis of Au NPs, 100 mg of trisodium citrate (0.34 mmol) was dissolved in 148 mL of deionized water in a round-bottom flask under boiling conditions (110 °C).[61] Then, 2 mL of $HauCl_4 \cdot 3H_2O$ solution (0.025 mmol) was added to this mixture, which was kept under magnetic stirring for over 30 min, enabling the formation of a red suspension containing Au NPs. AuPd NPs were synthesized by transferring 75 mL of the aqueous Au NP suspension obtained in the previous step to a round-bottom flask, followed by stirring at 70 °C for 20 min using a silicon bath. Then, 35.2 mg of L-ascorbic acid (0.2 mmol) was added to this suspension, followed by stirring for another 30 min. Then, 215 μL (0.658 μmol) or 21.5 μL (0.066 μmol) of K_2PdCl_4 solution (1 mg/mL) was added to the reaction mixture to form $Au_{97}Pd_3$ and $Au_{99.7}Pd_{0.3}$ NPs, respectively. Following the addition of the Pd precursor, the reaction mixture was kept at 70 °C with stirring for another 30 min. The NPs were then washed with water by successive rounds of centrifugation and removal of the supernatant. We also prepared AuPd NPs supported on SiO_2 (3 wt % in terms of metal) to perform XRD and CO-TPD characterization. In this case, the pH of the AuPd NP suspension obtained in the previous step was adjusted to 3 by the addition of 20 μL of concentrated $HNO_{3(aq)}$. This was followed by the addition of 100 mg of nanosilica powder and stirring for 12 h at 70 °C to produce AuPd/SiO_2 samples. The AuPd/SiO_2 NPs were isolated by centrifugation for 20 min at 7500 rpm and washed twice with water by successive rounds of centrifugation and removal of the supernatant, and the mixture was dried at 70 °C.

Electrocatalytic Studies: Nitrite Reduction Reaction (NO_2RR). Electrochemical experiments were performed in a three-electrode glass cell, with a glassy carbon rod (GCE) used as a working electrode (6 mm diameter, geometric area of 0.2827 cm^2) and a high area graphite rod used as a counter electrode. All of the potentials were measured and displayed based on the reversible hydrogen electrode (RHE) prepared with the same solution of the supporting electrolyte (0.1 M $HClO_4$). The GCE electrode was purified by polishing with alumina slurry and sonicating in ultrapure water and acetone (5 min each). To avoid residual contamination from the synthesis, the NPs were cleaned twice by washing them with water to remove synthesis reactants. After that, the clean GCE was modified by drop casting 30 μL of catalyst ink (AuPd nanoparticles and carbon black Vulcan XC−72R dispersed in H_2O: IPA solution), resulting in a uniform film with a Au loading of 200 μg/cm^2 and Vulcan carbon loading of 100 μg/cm^2.

The electrochemical measurements were carried out at room temperature (25 °C), using an Autolab PGSTAT 128 N equipped with a Scan 250 modulus as a potentiostat. Before the experiments, the solution was purged with Argon 2.2, which was kept in the cell headspace during the data collection. The plasmonic excitation was performed by irradiating the electrochemical cell with one Kessil PR 160L LED with 525 nm as the light wavelength (total irradiance of 59.50 mW cm^{-2}). For electrocatalytic studies, cyclic voltammograms were normalized by the palladium mass present in each catalyst, according to the results of atomic emission spectroscopy experiments (MP-AES). The data normalized by the geometric area are also provided.

For the NO_2RR studies, the supporting electrolyte was prepared by diluting $HClO_4$ directly into 18.2 MΩ cm of water. Sodium nitrite was then added to the electrolyte from a 1 M stock solution to achieve the target concentration as described in the text. Cyclic voltammetry (CV) measurements were performed at a scan rate of 10 mV s^{-1}, and chronoamperometric analysis (CA) measurements were recorded at 0.050 V (vs RHE) under chopped illumination, both in Ar-saturated 0.1 M $HClO_4$ solution.

The indophenol method was used to determine the NH_3 concentration produced by the nitrite conversion.[33] The CA measurements were performed at 0.05 V for 1 h using an electrochemical cell with a controllable warm water bath at 25 °C through a Julabo F12−MA refrigerated circulator to avoid the temperature variation. Briefly, considering that the indophenol reaction is pH-dependent, sodium hydroxide solution was added to the electrolyte to achieve an alkaline pH. Five mL portion of electrolyte was mixed with 600 μL of 2.75 M sodium salicylate and 0.95 mM sodium nitroprusside solution. The resultant solution was kept in the dark for 45 min after the addition of 1 mL of solution containing 306 mM sodium citrate, 418 mM sodium hydroxide, and 1.5 mM sodium hypochlorite (10% active chlorine basis). The indophenol dye formed after the reaction between ammonium ion and salicylate (see the mechanism proposed by Krom[3]) can be determined by the 650 nm band in the UV−Vis spectra. The absorbance at 650 nm was plotted against a calibration curve to calculate the NH_3 concentration.

ASSOCIATED CONTENT

Supporting Information

The Supporting Information is available free of charge at https://pubs.acs.org/doi/10.1021/acsnano.4c07076.

Additional characterization (MP-AES, electron microscopy data and modeling, histograms of size distribution, XPS, LSVs); catalytic data (LSVs, UV−vis); and computational modeling (PDF)

AUTHOR INFORMATION

Corresponding Authors

Wenyi Huo − *College of Mechanical and Electrical Engineering, Nanjing Forestry University, Nanjing 210037, P.*

https://doi.org/10.1021/acsnano.4c07076
ACS Nano 2024, 18, 24391−24403

R. China; NOMATEN Centre of Excellence, National Centre for Nuclear Research, Otwock 05-400, Poland; orcid.org/0000-0001-8297-9045; Email: wyhuo@njfu.edu.cn

Sarah J. Haigh − *Department of Materials, University of Manchester, Manchester M13 9PL, United Kingdom;* orcid.org/0000-0001-5509-6706; Email: sarah.haigh@manchester.ac.uk

Pedro H. C. Camargo − *Department of Chemistry, University of Helsinki, FIN-0014 Helsinki, Finland;* orcid.org/0000-0002-7815-7919; Email: pedro.camargo@helsinki.fi

Authors

Kaline N. da Silva − *Department of Chemistry, University of Helsinki, FIN-0014 Helsinki, Finland;* orcid.org/0000-0001-8077-146X

Shwetha Shetty − *Department of Chemistry, University of Helsinki, FIN-0014 Helsinki, Finland*

Sam Sullivan−Allsop − *Department of Materials, University of Manchester, Manchester M13 9PL, United Kingdom*

Rongsheng Cai − *Department of Materials, University of Manchester, Manchester M13 9PL, United Kingdom*

Shiqi Wang − *Department of Chemistry, University of Helsinki, FIN-0014 Helsinki, Finland*

Jhon Quiroz − *Department of Chemistry, University of Helsinki, FIN-0014 Helsinki, Finland*

Mykhailo Chundak − *Department of Chemistry, University of Helsinki, FIN-0014 Helsinki, Finland*

Hugo L. S. dos Santos − *Department of Chemistry, University of Helsinki, FIN-0014 Helsinki, Finland*

IbrahiM Abdelsalam − *Department of Chemistry, University of Helsinki, FIN-0014 Helsinki, Finland*

Freddy E. Oropeza − *Photoactivated Processes Unit, IMDEA Energy Institute, 28935 Mostoles, Madrid, Spain;* orcid.org/0000-0001-7222-9603

Víctor A. de la Peña O'Shea − *Photoactivated Processes Unit, IMDEA Energy Institute, 28935 Mostoles, Madrid, Spain;* orcid.org/0000-0001-5762-4787

Niko Heikkinen − *VTT Technical Research Centre of Finland, FIN-02044 Espoo, Finland;* orcid.org/0000-0002-9788-1291

Elton Sitta − *Department of Chemistry, Federal University of Sao Carlos, Sao Carlos 13565−905, Brazil;* orcid.org/0000-0003-3181-0076

Tiago V. Alves − *Departamento de Físico-Química, Instituto de Química, Universidade Federal da Bahia, 14740170-115 Salvador, BA, Brazil;* orcid.org/0000-0001-9129-3272

Mikko Ritala − *Department of Chemistry, University of Helsinki, FIN-0014 Helsinki, Finland;* orcid.org/0000-0002-6210-2980

Thomas J. A. Slater − *Cardiff Catalysis Institute, School of Chemistry, Cardiff University, Cardiff CF10 3AT, United Kingdom;* orcid.org/0000-0003-0372-1551

Complete contact information is available at: https://pubs.acs.org/10.1021/acsnano.4c07076

Notes

The authors declare no competing financial interest.

ACKNOWLEDGMENTS

This work was supported by the Jane and Aatos Erkko Foundation and the Academy of Finland (decision no. 334826). S.J.H. acknowledges funding from EPSRC (EP/P009050/1) and the European Research Council under the Horizon 2020 program for the ERC Starter Grant EvoluTEM (715502). TEM access for this work was supported by the Henry Royce Institute for Advanced Materials, funded through EPSRC grants EP/R00661X/1, EP/S019367/1, EP/P025021/1, and EP/P025498/1. ES thanks the Sao Paulo Research Foundation (FAPESP, #2013/07296-2, #2017/11986-5) and Brazilian Council for Scientific and Technological Development (CNPq, 405752/2022-9) for financial support (310550/2022-0). K.N.d.S. thanks the National Council for the Improvement of Higher Education for the scholarship (Capes—PrInt 88887.464913/2019-00). EU/Interreg Aurora/Sustainable Hydrogen project is also acknowledged for its financial support. This work was partly supported by the European Union Horizon 2020 research and innovation program under the NOMATEN Teaming grant (857470) and the European Regional Development Fund via the Foundation for Polish Science International Research Agenda PLUS program grant (MAB PLUS/2018/8). The publication was created partly within the framework of the project of the Minister of Science and Higher Education "Support for the activities of Centres of Excellence established in Poland under Horizon 2020" under contract no. MEiN/2023/DIR/3795. F.E.O. thanks the RYC2021-034254-I grant funded by MCIN/AEI/10.13039/501100011033 and by the "European Union NextGenerationEU/PRTR". Facilities of ALD center Finland research infrastructure were used for XPS characterization.

REFERENCES

(1) Aslam, U.; Rao, V. G.; Chavez, S.; Linic, S. Catalytic Conversion of Solar to Chemical Energy on Plasmonic Metal Nanostructures. *Nat. Catal.* **2018**, *1*, 656−665.

(2) *Plasmonic Catalysis From Fundamentals to Applications*, 1st ed.; Camargo, P. H.; Cortes, E., Eds.; WILEY-VCH GmbH: Weinheim, 2021.

(3) Gellé, A.; Jin, T.; De La Garza, L.; Price, G. D.; Besteiro, L. V.; Moores, A. Applications of Plasmon-Enhanced Nanocatalysis to Organic Transformations. *Chem. Rev.* **2020**, *120*, 986−1041.

(4) Zhou, L.; Swearer, D. F.; Zhang, C.; Robatjazi, H.; Zhao, H.; Henderson, L.; Dong, L.; Christopher, P.; Carter, E. A.; Nordlander, P.; Halas, N. J. Quantifying Hot Carrier and Thermal Contributions in Plasmonic Photocatalysis. *Science* **2018**, *362*, 69−72.

(5) Cortés, E.; Besteiro, L. V.; Alabastri, A.; Baldi, A.; Tagliabue, G.; Demetriadou, A.; Narang, P. Challenges in Plasmonic Catalysis. *ACS Nano* **2020**, *14*, 16202−16219.

(6) Peiris, E.; Hanauer, S.; Le, T.; Wang, J.; Salavati-fard, T.; Brasseur, P.; Formo, E. V.; Wang, B.; Camargo, P. H. C. Controlling Selectivity in Plasmonic Catalysis: Switching Reaction Pathway from Hydrogenation to Homocoupling Under Visible-Light Irradiation. *Angew. Chem., Int. Ed.* **2023**, *62*, No. e202216398.

(7) Dong, Y.; Hu, C.; Xiong, H.; Long, R.; Xiong, Y. Plasmonic Catalysis: New Opportunity for Selective Chemical Bond Evolution. *ACS Catal.* **2023**, *13*, 6730−6743.

(8) Quiroz, J.; Barbosa, E. C. M. M.; Araujo, T. P.; Fiorio, J. L.; Wang, Y.-C. C.; Zou, Y.-C. C.; Mou, T.; Alves, T. V.; De Oliveira, D. C.; Wang, B.; Haigh, S. J.; Rossi, L. M.; Camargo, P. H. C. C. Controlling Reaction Selectivity over Hybrid Plasmonic Nanocatalysts. *Nano Lett.* **2018**, *18*, 7289−7297.

(9) Araujo, T. P.; Quiroz, J.; Barbosa, E. C. M.; Camargo, P. H. C. Understanding Plasmonic Catalysis with Controlled Nanomaterials Based on Catalytic and Plasmonic Metals. *Curr. Opin. Colloid Interface Sci.* **2019**, *39*, 110−122.

(10) Swearer, D. F.; Zhao, H.; Zhou, L.; Zhang, C.; Robatjazi, H.; Martirez, J. M. P.; Krauter, C. M.; Yazdi, S.; McClain, M. J.; Ringe, E.; Carter, E. A.; Nordlander, P.; Halas, N. J. Heterometallic Antenna-Reactor Complexes for Photocatalysis. *Proc. Natl. Acad. Sci. U.S.A.* **2016**, *113*, 8916−8920.

(11) Zhou, L.; Martirez, J. M. P.; Finzel, J.; Zhang, C.; Swearer, D. F.; Tian, S.; Robatjazi, H.; Lou, M.; Dong, L.; Henderson, L.; Christopher, P.; Carter, E. A.; Nordlander, P.; Halas, N. J. Light-Driven Methane Dry Reforming with Single Atomic Site Antenna-Reactor Plasmonic Photocatalysts. *Nat. Energy* **2020**, *5*, 61−70.
(12) Li, K.; Hogan, N. J.; Kale, M. J.; Halas, N. J.; Nordlander, P.; Christopher, P. Balancing Near-Field Enhancement, Absorption, and Scattering for Effective Antenna-Reactor Plasmonic Photocatalysis. *Nano Lett.* **2017**, *17*, 3710−3717.
(13) Quiroz, J.; Barbosa, E. C. M.; Araujo, T. P.; Fiorio, J. L.; Wang, Y. C.; Zou, Y. C.; Mou, T.; Alves, T. V.; De Oliveira, D. C.; Wang, B.; Haigh, S. J.; Rossi, L. M.; Camargo, P. H. C. Controlling Reaction Selectivity over Hybrid Plasmonic Nanocatalysts. *Nano Lett.* **2018**, *18*, 7289−7297.
(14) Aslam, U.; Chavez, S.; Linic, S. Controlling Energy Flow in Multimetallic Nanostructures for Plasmonic Catalysis. *Nat. Nanotechnol.* **2017**, *12*, 1000−1005.
(15) Chavez, S.; Aslam, U.; Linic, S. Design Principles for Directing Energy and Energetic Charge Flow in Multicomponent Plasmonic Nanostructures. *ACS Energy Lett.* **2018**, *3*, 1590−1596.
(16) Lee, S.; Hwang, H.; Lee, W.; Schebarchov, D.; Wy, Y.; Grand, J.; Auguié, B.; Wi, D. H.; Cortés, E.; Han, S. W. Core−Shell Bimetallic Nanoparticle Trimers for Efficient Light-to-Chemical Energy Conversion. *ACS Energy Lett.* **2020**, *5*, 3881−3890.
(17) Long, R.; Li, Y.; Song, L.; Xiong, Y. Coupling Solar Energy into Reactions: Materials Design for Surface Plasmon-Mediated Catalysis. *Small* **2015**, *11*, 3873−3889.
(18) Huang, H.; Zhang, L.; Lv, Z.; Long, R.; Zhang, C.; Lin, Y.; Wei, K.; Wang, C.; Chen, L.; Li, Z. Y.; Zhang, Q.; Luo, Y.; Xiong, Y. Unraveling Surface Plasmon Decay in Core-Shell Nanostructures toward Broadband Light-Driven Catalytic Organic Synthesis. *J. Am. Chem. Soc.* **2016**, *138*, 6822−6828.
(19) Verma, R.; Tyagi, R.; Voora, V. K.; Polshettiwar, V. Black Gold-Based "Antenna-Reactor" To Activate Non-Plasmonic Nickel: Photocatalytic Hydrodechlorination and Hydrogenation Reactions. *ACS Catal.* **2023**, *13*, 7395−7406.
(20) Robatjazi, H.; Zhao, H.; Swearer, D. F.; Hogan, N. J.; Zhou, L.; Alabastri, A.; McClain, M. J.; Nordlander, P.; Halas, N. J. Plasmon-Induced Selective Carbon Dioxide Conversion on Earth-Abundant Aluminum-Cuprous Oxide Antenna-Reactor Nanoparticles. *Nat. Commun.* **2017**, *8*, No. 27.
(21) Gargiulo, J.; Herran, M.; Violi, I. L.; Sousa-Castillo, A.; Martinez, L. P.; Ezendam, S.; Barella, M.; Giesler, H.; Grzeschik, R.; Schlücker, S.; Maier, S. A.; Stefani, F. D.; Cortés, E. Impact of Bimetallic Interface Design on Heat Generation in Plasmonic Au/Pd Nanostructures Studied by Single-Particle Thermometry. *Nat. Commun.* **2023**, *14*, No. 3813.
(22) Dropsch, H.; Baerns, M. CO Adsorption on Supported Pd Catalysts Studied by Adsorption Microcalorimetry and Temperature Programmed Desorption. *Appl. Catal., A* **1997**, *158*, 163−183.
(23) Föhlisch, A.; Nyberg, M.; Bennich, P.; Triguero, L.; Hasselström, J.; Karis, O.; Pettersson, L. G. M.; Nilsson, A. The Bonding of CO to Metal Surfaces. *J. Chem. Phys.* **2000**, *112*, 1946−1958.
(24) Abbott, H. L.; Aumer, A.; Lei, Y.; Asokan, C.; Meyer, R. J.; Sterrer, M.; Shaikhutdinov, S.; Freund, H. J. CO Adsorption on Monometallic and Bimetallic Au-Pd Nanoparticles Supported on Oxide Thin Films. *J. Phys. Chem. C* **2010**, *114*, 17099−17104.
(25) Huang, R.; Kim, K.; Kim, H. J.; Jang, M. G.; Han, J. W. Size-Controlled Pd Nanoparticles Loaded on Co3O4 Nanoparticles by Calcination for Enhanced CO Oxidation. *ACS Appl. Nano Mater.* **2020**, *3*, 486−495.
(26) Liu, J.; Shan, J.; Lucci, F. R.; Cao, S.; Sykes, E. C. H.; Flytzani-Stephanopoulos, M. Palladium-Gold Single Atom Alloy Catalysts for Liquid Phase Selective Hydrogenation of 1-Hexyne. *Catal. Sci. Technol.* **2017**, *7*, 4276−4284.
(27) Kalita, G. D.; Sarmah, P. P.; Kalita, G.; Das, P. Bimetallic Au−Pd Nanoparticles Supported on Silica with a Tunable Core@shell Structure: Enhanced Catalytic Activity of Pd(Core)−Au(Shell) over Au(Core)−Pd(Shell). *Nanoscale Adv.* **2021**, *3*, 5399−5416.
(28) Khawaji, M.; Chadwick, D. Au−Pd NPs Immobilised on Nanostructured Ceria and Titania: Impact of Support Morphology on the Catalytic Activity for Selective Oxidation. *Catal. Sci. Technol.* **2018**, *8*, 2529−2539.
(29) Venäläinen, A.; Meinander, K.; Räisänen, M.; Tuboltsev, V.; Räisänen, J. Metallization of Self-Assembled Organic Monolayer Surfaces by Pd Nanocluster Deposition. *Surf. Sci.* **2018**, *677*, 68−77.
(30) da Silva, K. N.; Soffiati, G.; da Silva, E. Z.; San-Miguel, M. A.; Sitta, E. Using the Site-Knockout Strategy to Understand the Low Activity of the Nitrate Electro-Reduction Reaction on Pt(111). *New J. Chem.* **2022**, *46*, 12132−12138.
(31) Wilson, A. J.; Mohan, V.; Jain, P. K. Mechanistic Understanding of Plasmon-Enhanced Electrochemistry. *J. Phys. Chem. C* **2019**, *123*, 29360−29369.
(32) Chun, H. J.; Apaja, V.; Clayborne, A.; Honkala, K.; Greeley, J. Atomistic Insights into Nitrogen-Cycle Electrochemistry: A Combined DFT and Kinetic Monte Carlo Analysis of NO Electrochemical Reduction on Pt(100). *ACS Catal.* **2017**, *7*, 3869−3882.
(33) Krom, M. D. Spectrophotometric Determination of Ammonia: A Study of a Modified Berthelot Reaction Using Salicylate and Dichloroisocyanurate. *Analyst* **1980**, *105*, 305−316.
(34) Linic, S.; Christopher, P.; Ingram, D. B. Plasmonic-Metal Nanostructures for Efficient Conversion of Solar to Chemical Energy. *Nat. Mater.* **2011**, *10*, 911−921.
(35) Zhao, J.; Xue, S.; Ji, R.; Li, B.; Li, J. Localized Surface Plasmon Resonance for Enhanced Electrocatalysis. *Chem. Soc. Rev.* **2021**, *50*, 12070−12097.
(36) Kamarudheen, R.; Aalbers, G. J. W.; Hamans, R. F.; Kamp, L. P. J.; Baldi, A. Distinguishing among All Possible Activation Mechanisms of a Plasmon-Driven Chemical Reaction. *ACS Energy Lett.* **2020**, *5*, 2605−2613.
(37) Contreras, E.; Nixon, R.; Litts, C.; Zhang, W.; Alcorn, F. M.; Jain, P. K. Plasmon-Assisted Ammonia Electrosynthesis. *J. Am. Chem. Soc.* **2022**, *144*, 10743−10751.
(38) Singh, S.; Verma, R.; Kaul, N.; Sa, J.; Punjal, A.; Prabhu, S.; Polshettiwar, V. Surface Plasmon-Enhanced Photo-Driven CO2 Hydrogenation by Hydroxy-Terminated Nickel Nitride Nanosheets. *Nat. Commun.* **2023**, *14*, No. 2551.
(39) Zheng, Z.; Tachikawa, T.; Majima, T. Plasmon-Enhanced Formic Acid Dehydrogenation Using Anisotropic Pd-Au Nanorods Studied at the Single-Particle Level. *J. Am. Chem. Soc.* **2015**, *137*, 948−957.
(40) Forcherio, G. T.; Ostovar, B.; Boltersdorf, J.; Cai, Y. Y.; Leff, A. C.; Grew, K. N.; Lundgren, C. A.; Link, S.; Baker, D. R. Single-Particle Insights into Plasmonic Hot Carrier Separation Augmenting Photoelectrochemical Ethanol Oxidation with Photocatalytically Synthesized Pd-Au Bimetallic Nanorods. *ACS Nano* **2022**, *16*, 12377−12389.
(41) Verma, R.; Belgamwar, R.; Chatterjee, P.; Bericat-Vadell, R.; Sa, J.; Polshettiwar, V. Nickel-Laden Dendritic Plasmonic Colloidosomes of Black Gold: Forced Plasmon Mediated Photocatalytic CO2 Hydrogenation. *ACS Nano* **2023**, *17*, 4526−4538.
(42) Peiris, E.; Hanauer, S.; Le, T.; Wang, J.; Salavati-fard, T.; Brasseur, P.; Formo, E. V.; Wang, B.; Camargo, P. H. C. Controlling Selectivity in Plasmonic Catalysis: Switching Reaction Pathway from Hydrogenation to Homocoupling Under Visible-Light Irradiation. *Angew. Chem. Int. Ed* **2023**, *62*, No. e202216398.
(43) Peiris, E.; Sarina, S.; Waclawik, E. R.; Ayoko, G. A.; Han, P.; Jia, J.; Zhu, H. Y. Plasmonic Switching of the Reaction Pathway: Visible-Light Irradiation Varies the Reactant Concentration at the Solid−-Solution Interface of a Gold−Cobalt Catalyst. *Angew. Chem. Int. Ed* **2019**, *58*, 12032−12036.
(44) Zhang, X.; Li, X.; Zhang, D.; Su, N. Q.; Yang, W.; Everitt, H. O.; Liu, J. Product Selectivity in Plasmonic Photocatalysis for Carbon Dioxide Hydrogenation. *Nat. Commun.* **2017**, *8*, No. 14542.

https://doi.org/10.1021/acsnano.4c07076
ACS Nano 2024, 18, 24391−24403

(45) Yu, S.; Jain, P. K. Selective Branching of Plasmonic Photosynthesis into Hydrocarbon Production and Hydrogen Generation. *ACS Energy Lett.* **2019**, *4* (9), 2295−2300.
(46) De Marchi, S.; Núñez-Sánchez, S.; Bodelón, G.; Pérez-Juste, J.; Pastoriza-Santos, I. Pd Nanoparticles as a Plasmonic Material: Synthesis, Optical Properties and Applications. *Nanoscale* **2020**, *12* (46), 23424−23443.
(47) Wen, Q.; Duan, J.; Wang, W.; Huang, D.; Liu, Y.; Shi, Y.; Fang, J. K.; Nie, A.; Li, H.; Zhai, T. Engineering a Local Free Water Enriched Microenvironment for Surpassing Platinum Hydrogen Evolution Activity. *Angew. Chem., Int. Ed.* **2022**, *61* (35), No. e202206077.
(48) Hu, C.; Chen, X.; Low, J.; Yang, Y. W.; Li, H.; Wu, D.; Chen, S.; Jin, J.; Li, H.; Ju, H.; Wang, C. H.; Lu, Z.; Long, R.; Song, L.; Xiong, Y. Near-Infrared-Featured Broadband CO2 Reduction with Water to Hydrocarbons by Surface Plasmon. *Nat. Commun.* **2023**, *14*, No. 221, DOI: 10.1038/s41467-023-35860-2.
(49) Wang, Y.; Hu, J.; Ge, T.; Chen, F.; Lu, Y.; Chen, R.; Zhang, H.; Ye, B.; Wang, S.; Zhang, Y.; Ma, T.; Huang, H. Gradient Cationic Vacancies Enabling Inner-To-Outer Tandem Homojunctions: Strong Local Internal Electric Field and Reformed Basic Sites Boosting CO2 Photoreduction. *Adv. Mater.* **2023**, *35*, No. 2302538.
(50) Jia, G.; Sun, M.; Wang, Y.; Shi, Y.; Zhang, L.; Cui, X.; Huang, B.; Yu, J. C. Asymmetric Coupled Dual-Atom Sites for Selective Photoreduction of Carbon Dioxide to Acetic Acid. *Adv. Funct. Mater.* **2022**, *32*, No. 2206817.
(51) Tong, W.; Huang, B.; Wang, P.; Li, L.; Shao, Q.; Huang, X. Crystal-Phase-Engineered PdCu Electrocatalyst for Enhanced Ammonia Synthesis. *Angew. Chem. Int. Ed.* **2020**, *59*, 2649−2653.
(52) Li, L.; Bu, L.; Huang, B.; Wang, P.; Shen, C.; Bai, S.; Chan, T.-S.; Shao, Q.; Hu, Z.; Huang, X. Compensating Electronic Effect Enables Fast Site-to-Site Electron Transfer over Ultrathin RuMn Nanosheet Branches toward Highly Electroactive and Stable Water Splitting. *Adv. Mater.* **2021**, *33*, No. 2105308.
(53) Wei, J.; Xiao, K.; Chen, Y.; Guo, X. P.; Huang, B.; Liu, Z. Q. In Situ Precise Anchoring of Pt Single Atoms in Spinel Mn3O4 for a Highly Efficient Hydrogen Evolution Reaction. *Energy Environ. Sci.* **2022**, *15*, 4592−4600.
(54) Wang, J.; Huang, B.; Ji, Y.; Sun, M.; Wu, T.; Yin, R.; Zhu, X.; Li, Y.; Shao, Q.; Huang, X. A General Strategy to Glassy M-Te (M = Ru, Rh, Ir) Porous Nanorods for Efficient Electrochemical N2 Fixation. *Adv. Mater.* **2020**, *32*, No. 1907112.
(55) Li, Y.; Yang, C.; Ge, C.; Yao, N.; Yin, J.; Jiang, W.; Cong, H.; Cheng, G.; Luo, W.; Zhuang, L. Electronic Modulation of Ru Nanosheet by d−d Orbital Coupling for Enhanced Hydrogen Oxidation Reaction in Alkaline Electrolytes. *Small* **2022**, *18*, No. 2202404.
(56) *Hyperspy/Hyperspy: Release v1.6.3*, 10.5281/ZENODO.4923970. Accessed on August 5th, 2024.
(57) Ciezak, J. A.; Trevino, S. F. The Molecular Structure and Inelastic Neutron Scattering Spectra of 2,6-Diamino-3,5-Dinitropyrazine. *J. Mol. Struct.* **2005**, *723*, 241−244.
(58) Perdew, J. P.; Burke, K.; Ernzerhof, M. Generalized Gradient Approximation Made Simple. *Phys. Rev. Lett.* **1996**, *77*, 3865.
(59) Grimme, S.; Antony, J.; Ehrlich, S.; Krieg, H. A Consistent and Accurate Ab Initio Parametrization of Density Functional Dispersion Correction (DFT-D) for the 94 Elements H-Pu. *J. Chem. Phys.* **2010**, *132*, No. 154104.
(60) Nørskov, J. K.; Rossmeisl, J.; Logadottir, A.; Lindqvist, L.; Kitchin, J. R.; Bligaard, T.; Jónsson, H. Origin of the Overpotential for Oxygen Reduction at a Fuel-Cell Cathode. *J. Phys. Chem. B* **2004**, *108*, 17886−17892.
(61) Kimling, J.; Maier, M.; Okenve, B.; Kotaidis, V.; Ballot, H.; Plech, A. Turkevich Method for Gold Nanoparticle Synthesis Revisited. *J. Phys. Chem. B* **2006**, *110*, 15700−15707.

https://doi.org/10.1021/acsnano.4c07076
ACS Nano 2024, 18, 24391−24403